CrossMark

Turbulent Energy Transfer and Proton–Electron Heating in Collisionless Plasmas

S. Roy[1] , R. Bandyopadhyay[2] , Y. Yang[1] , T. N. Parashar[3] , W. H. Matthaeus[1] , S. Adhikari[1] , V. Roytershteyn[4] ,
A. Chasapis[5] , Hui Li[6,7] , D. J. Gershman[8] , B. L. Giles[8] , and J. L. Burch[9]
[1] Department of Physics and Astronomy, University of Delaware, Newark, DE 19716, USA
[2] Department of Astrophysical Sciences, Princeton University, Princeton, NJ 08544, USA; riddhib@princeton.edu
[3] Victoria University of Wellington, New Zealand
[4] Space Science Institute, Boulder, CO 80301, USA
[5] Laboratory for Atmospheric and Space Physics, University of Colorado Boulder, Boulder, CO 80309, USA
[6] State Key Laboratory of Space Weather, National Space Science Center, CAS, Beijing, 100190, People's Republic of China
[7] University of Chinese Academy of Sciences, Beijing, 100049, People's Republic of China
[8] NASA Goddard Space Flight Center, Greenbelt, MD 20771, USA
[9] Southwest Research Institute, San Antonio, TX 78238, USA
Received 2022 May 4; revised 2022 November 16; accepted 2022 November 18; published 2022 December 19

Abstract

Despite decades of study of high-temperature weakly collisional plasmas, a complete understanding of how energy is transferred between particles and fields in turbulent plasmas remains elusive. Two major questions in this regard are how fluid-scale energy transfer rates, associated with turbulence, connect with kinetic-scale dissipation, and what controls the fraction of dissipation on different charged species. Although the rate of cascade has long been recognized as a limiting factor in the heating rate at kinetic scales, there has not been direct evidence correlating the heating rate with MHD-scale cascade rates. Using kinetic simulations and in situ spacecraft data, we show that the fluid-scale energy flux indeed accounts for the total energy dissipated at kinetic scales. A phenomenology, based on disruption of proton gyromotion by fluctuating electric fields that are produced in turbulence at proton scales, argues that the proton versus electron heating is controlled by the ratio of the nonlinear timescale to the proton cyclotron time and by the plasma beta. The proposed scalings are supported by the simulations and observations.

Unified Astronomy Thesaurus concepts: Plasma physics (2089); Space plasmas (1544); Magnetohydrodynamics (1964); Plasma astrophysics (1261)

1. Introduction

Most heliospheric and astrophysical plasmas are considered to exist in a turbulent state (Matthaeus & Velli 2011). A classical turbulent system, as in hydrodynamics (Monin & Yaglom 1971) or magnetohydrodynamics (MHD, Verma 2004), transfers energy from large scales to progressively smaller scales until it is ultimately dissipated as heat—a process that, in steady state and at high Reynolds number, is known as the energy cascade. The nature of energy dissipation by nonlinear cascade and its effects on turbulent plasma are of central interest in space physics and astrophysics. Prominent examples include understanding the heating of the solar corona and solar wind, acceleration and transport of energetic particles, and dynamo generation of magnetic fields (e.g., Montgomery et al. 1980; Bruno & Carbone 2005; Matthaeus & Velli 2011; Verscharen et al. 2019). Despite its importance and compelling nature, the nature of energy cascade and dissipation in turbulent, weakly collisional plasmas is not well understood.

The complications that arise in a plasma in the limit of weak or vanishing collisions can be framed in terms of a Boltzmann–Maxwell system as it transitions to a Vlasov–Maxwell system. The Boltzmann system, unlike the full many-body problem, has already lost the reversibility that characterizes classical (elastic) collisions. The commonly employed collision operators render the system irreversible, not the collisions themselves. Nevertheless, collisional closures such as resistivity and viscosity introduce a convenient closure that imposes irreversibility and a precise parameterization of where and when dissipation occurs. Standard viscosity and resistivity connect macroscopic processes—the mechanisms that produce enhancements of electric current density, compressions, and rate of strain—to the production of internal energy. Lacking collisional closures, the association of dissipation to specific plasma processes becomes more problematic. For more discussion of this, see Verscharen et al. (2019) and Matthaeus et al. (2020).

The above challenges have motivated various efforts to identify the specific mechanisms involved in collisionless dissipation. Several heating mechanisms such as Landau/transit-time resonances (Chen et al. 2019; Afshari et al. 2021), stochastic heating (Chandran et al. 2010; Hoppock et al. 2018), cyclotron resonances (Gary et al. 1995; Isenberg et al. 2001), kinetic instabilities, and magnetic pumping (Lichko et al. 2017) have been proposed as contributing candidates. Another approach, adopted here, focuses more broadly on the general discussion of the pathways leading to dissipation: transfer across scales, transfer between particles and electromagnetic fields, and transfer between flow energies and internal energies for each species.

In idealized circumstances the cascade begins with the large scales and continues through the inertial range described by statistical theories (Kolmogorov 1941), and then through complex plasma processes into the dissipation range. Though MHD theories adequately describe many aspects of the processes at energy-containing and inertial scales (Montgomery 1983; Goldstein et al. 1995; Parashar et al. 2015), they fail to explain the small-scale processes that drive dissipation

(Barnes 1979; Marsch 1991, 2006). This paper bridges the MHD and kinetic measures of turbulent heating rate in a statistical way.

2. The Role of Pressure–Strain Interaction in Dissipation

The transfer and conversion of energy from turbulent magnetic fluctuations to particles is realized through particle–field interactions. Such transfer occurs only due to $\boldsymbol{j} \cdot \boldsymbol{E}$, and this term is responsible for conversion of electromagnetic energy into kinetic energy (Zenitani et al. 2011). Here $\boldsymbol{E}$ is the electric field and $\boldsymbol{j}$ is the current density. Traditionally, this $\boldsymbol{j} \cdot \boldsymbol{E}$ term, often called the electromagnetic work on particles, has been used as the standard measure of energy dissipation in space plasma research. However, a simple treatment of the Vlasov–Maxwell system of equations highlights the more specific effect of $\boldsymbol{j} \cdot \boldsymbol{E}$ and reveals the role of a term involving pressure–strain interaction in energy conversion.

The energy per unit volume in a plasma can be divided into three categories (see Braginskii 1965; Freidberg 1982): $\mathcal{E}_s^f =$ bulk flow kinetic energy, $\mathcal{E}_s^{\text{th}} =$ random or internal energy, and $\mathcal{E}^m =$ electromagnetic energy. From the hierarchy of the moments of the Vlasov–Maxwell equations, one finds (Cerri 2016; Yang et al. 2017a, 2017b; Sitnov et al. 2018), for each particle species, here labeled by s,

$$\partial_t \mathcal{E}_s^f + \nabla \cdot (\mathcal{E}_s^f \boldsymbol{u}_s + \boldsymbol{P}_s \cdot \boldsymbol{u}_s) = (\boldsymbol{P}_s \cdot \nabla) \cdot \boldsymbol{u}_s + n_s q_s \boldsymbol{E} \cdot \boldsymbol{u}_s, \tag{1}$$

$$\partial_t \mathcal{E}_s^{\text{th}} + \nabla \cdot (\mathcal{E}_s^{\text{th}} \boldsymbol{u}_s + \boldsymbol{h}_s) = -(\boldsymbol{P}_s \cdot \nabla) \cdot \boldsymbol{u}_s, \tag{2}$$

$$\partial_t \mathcal{E}^m + (c/4\pi)\nabla \cdot (\boldsymbol{E} \times \boldsymbol{B}) = -\boldsymbol{j} \cdot \boldsymbol{E}, \tag{3}$$

where $q_s =$ charge, $n_s =$ number density, $\boldsymbol{u}_s =$ fluid flow (bulk) velocity, $\boldsymbol{P}_s =$ pressure tensor, $\boldsymbol{h}_s =$ heat flux, $\boldsymbol{B} =$ magnetic field, $\boldsymbol{E} =$ electric field, and $\boldsymbol{j} = \sum_s n_s q_s \boldsymbol{u}_s$ is the net current density.

Dissipation is the conversion of some form of plasma energy into internal energy ($\mathcal{E}_s^{\text{th}}$). Let us ask the question, "Which terms in Equations (1) and (2) can cause this?" The divergence terms on the left side of each equation are responsible for transporting energy spatially but they do not convert energy from one form to another. Traditionally, the $\boldsymbol{j} \cdot \boldsymbol{E}$ term has been used as the standard measure of energy dissipation (e.g., Retinò et al. 2007; Zenitani et al. 2011; Wan et al. 2016). However, from Equations (1)–(3), $\boldsymbol{j} \cdot \boldsymbol{E}$ only converts energy between fields and the bulk flow, but not into the internal energy. The only term that converts (bulk flow) energy into internal energy is the pressure–strain interaction, $\text{PS}^{(s)} = -(\boldsymbol{P}_s \cdot \nabla) \cdot \boldsymbol{u}_s$. This is demonstrated in Figure 1, where we can see that the time-integrated pressure–strain rate closely follows the time history of the plasma internal energy, while the ohmic dissipation term does not (Yang et al. 2022).

The pressure–strain interaction can be further decomposed into two parts: $-(\boldsymbol{P} \cdot \nabla) \cdot \boldsymbol{u} = -p\theta - \Pi_{ij} D_{ij}$, where $p = \frac{1}{3}P_{ii}$, $\Pi_{ij} = P_{ij} - p\delta_{ij}$, $\theta = \nabla \cdot \boldsymbol{u}$, and $D_{ij} = \frac{1}{2}(\partial_i u_j + \partial_j u_i) - \frac{1}{3}\theta\delta_{ij}$. Here, δ_{ij} is the Kronecker delta function. The $p\theta$ term accounts for compressive heating and is known as the pressure-dilatation term. The second term, which combines the traceless parts of the pressure and the strain tensors, becomes the viscous term in the Chapman–Enskog expansion, but does not have a closure in the weakly collisional case. We designate this $-\Pi_{ij} D_{ij}$ term, including the minus sign, as the "Pi-D" interaction, defining $Pi - D^{(s)} \equiv -\Pi_{ij}^{(s)} D_{ij}^{(s)}$.
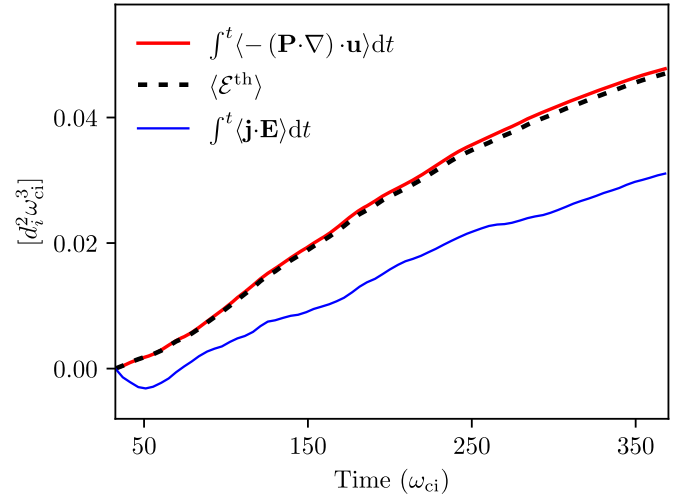
Figure 1. Time evolution of the total (proton + electron) internal energy $\mathcal{E}^{\text{th}} = \mathcal{E}_p^{\text{th}} + \mathcal{E}_e^{\text{th}}$, the time-integrated total (proton + electron) pressure–strain rate $-(\boldsymbol{P} \cdot \nabla) \cdot \boldsymbol{u} = -(\boldsymbol{P}_i \cdot \nabla) \cdot \boldsymbol{u}_i - (\boldsymbol{P}_e \cdot \nabla) \cdot \boldsymbol{u}_e$, and the time-integrated ohmic dissipation rate $\boldsymbol{j} \cdot \boldsymbol{E}$ from a fully kinetic, 2.5D particle-in-cell simulation using the code P3D (Zeiler et al. 2002). The time integration is performed from an initial time of $32.5\, \omega_{\text{ci}}$, and the difference in the internal energy from the initial time is shown. More details of the simulation can be found in the Appendix and in Parashar et al. (2018) and Adhikari et al. (2021).

While much more can be said about the dynamical role of the $-(\boldsymbol{P} \cdot \nabla) \cdot \boldsymbol{u}$ term (Equation (2)) in the balance of energy conversion (Del Sarto et al. 2016; Del Sarto & Pegoraro 2017), an important property for the present study is that this term accounts accurately for changes in the internal energy. Furthermore $-(\boldsymbol{P} \cdot \nabla) \cdot \boldsymbol{u}$ accounts well for the separate increases in each species' internal energy $\mathcal{E}_s^{\text{th}}$ (Pezzi et al. 2021; Yang et al. 2022), and upon further decomposition it can also account for compressive ($-p\theta$) versus incompressive ($-\Pi_{ij} D_{ij}$) heating (Chasapis et al. 2018; Wang et al. 2021; Yang et al. 2022).

3. MMS Data

An evaluation of the pressure–strain energy conversion rate requires accurate measurement of the full pressure tensor as well as computation of spatial derivatives down to kinetic scales (Dunlop et al. 1988; Paschmann & Daly 1998), which was not possible before the Magnetospheric Multiscale (MMS) mission (Burch et al. 2016). The MMS data set provides the first opportunity to study the pressure–strain heating rate using observational data (Chasapis et al. 2018; Bandyopadhyay et al. 2020, 2021; Wang et al. 2021).

For the analyses conducted in this paper, we use approximately 1100 burst-mode MMS magnetosheath intervals. Intervals after 2018 June have been discarded due to the unavailability of electron moments from MMS4, required to compute the electron dissipation rates. The data intervals are the same as those used in Li et al. (2020). We only consider intervals that are sufficiently long enough to compute correlation times, which is essential to compute the von Kármán decay rates and to obtain robust statistical averages. The paper by Li et al. (2020) uses 1841 intervals, from which we select approximately 1100 intervals based on these conditions.

4. Energy Injection and MHD-scale Cascade

It is well established that the energy-containing eddies control the heating rate in sufficiently large collisionless plasmas (e.g., Wu et al. 2013; Parashar et al. 2015). The standard von Kármán approach to compute the energy injection rate at the large scale (de Kármán & Howarth 1938) adapted to MHD (Hossain et al. 1995; Wan et al. 2012; Bandyopadhyay et al. 2019) provides an estimate of the energy injection rate

$$\epsilon_{vK}^{\pm} = \alpha_{\pm} \frac{(Z^{\pm})^2 Z^{\mp}}{L_{\pm}} \qquad (4)$$

where $\epsilon_{vK}^{\pm} = -\frac{1}{2}d(Z^{\pm})^2/dt$ are the Elsässer decay rates, $\alpha_{\pm}$ are proportionality constants, $Z^{\pm}$ are the Elsässer amplitudes, and $L_{\pm}$ are the corresponding similarity length scales, usually estimated as the correlation length. Assuming that the small-scale transfer processes operate rapidly (Batchelor 1953), a quasi-steady state is established at small scales, and the average energy decay rate is then given by $\epsilon_{vK} = (\epsilon_{vK}^{+} + \epsilon_{vK}^{-})/2$, where the subscript "vK" denotes the von Kármán phenomenology.

The Politano–Pouquet (Politano & Pouquet 1998a, 1998b; PP98) third-order law can be used to estimate the energy flux (say, ϵ_{PP98}) through the range of scales intermediate to the energy-containing and dissipative scales. This is usually referred to as the inertial range of scales. In isotropic form, the PP98 third-order law may be written as

$$Y_{\pm}(r) = -\frac{4}{3}\epsilon_{PP98}^{\pm} \, r \qquad (5)$$

where $\epsilon_{PP98}^{\pm}$ are the Elsässer-field cascade rates, and $Y_{\pm}(r) = \langle \hat{r}.\Delta Z^{\mp}(r)|\Delta Z^{\pm}(r)|^2 \rangle$ are the mixed third-order structure functions. The single-time spatial increments are defined as $\Delta Z^{\pm}(r) = Z^{\pm}(x + r) - Z^{\pm}(x)$. Single-spacecraft observations usually measure the time increments of the Elsässer fields $\Delta Z^{\pm}(\tau; t) = Z^{\pm}(t + \tau) - Z^{\pm}(t)$. In using Equation (5), the temporal lags τ are converted to spatial lags r using the Taylor hypothesis, $r = V_{SW}\tau$ with bulk plasma speed V_{SW}. The energy cascade rate is computed from the average $\epsilon_{PP98} = (\epsilon_{PP98}^{+} + \epsilon_{PP98}^{-})/2$.

The von Kármán and third-order laws have been shown to adequately quantify the energy decay rate in plasmas, using simulations (Wu et al. 2013; Parashar et al. 2015; Yang et al. 2018) and observations (Verma et al. 1995; MacBride et al. 2005, 2008; Stawarz et al. 2009). Here, we ask whether the two estimates of energy transfer rate—the injection rate given by the von Kármán law and the inertial range flux given by the PP98 law—balance each other. Each formalism has its own limitation and strength. The von Kármán decay law (Equation (4)) involves a proportionality constant (α), which may depend on several parameters, such as the Reynolds number, plasma beta, anisotropy, and compressibility (Wan et al. 2012; Bandyopadhyay et al. 2019). The Politano–Pouquet third-order law (Equation (5)) is free of such constants, but assumes isotropy. Assuming low cross-helicity, $\alpha = 4C_{\epsilon}/(9\sqrt{3})$, where C_{ϵ} is the dimensionless dissipation rate (Usmanov et al. 2014). For the magnetosheath, the effective Reynolds number lies approximately in the range $\sim$50–100 (e.g., Stawarz et al. 2022). This corresponds to $C_{\epsilon} \approx 0.468$ (Linkmann et al. 2015; Bandyopadhyay et al. 2018). Therefore, for low cross-helicity, $C_{\epsilon}^{+} \approx C_{\epsilon}^{-} \approx 0.234$,
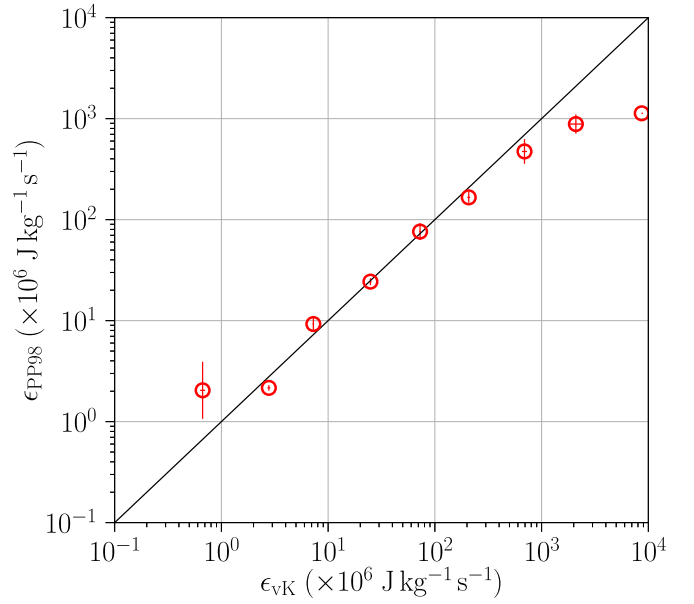
Figure 2. Comparison of the von Kármán decay rates and the inertial range flux derived from the Politano–Pouquet law for the MMS intervals. The computed rates were divided into nine bins and the averages in each bin are shown.

corresponding to a von Kármán constant value of $\alpha_{+} \approx \alpha_{-} \approx 0.06$. Using these values, we compute the energy decay rate using the two formulae for the $\sim$1100 magnetosheath intervals. The helicity barrier (Smith et al. 2009; Squire et al. 2022) may be important in systems with high cross-helicity, such as the near-Sun solar wind. However, in the collection of intervals used in our analysis, we found that about 95% of the intervals have cross-helicity of magnitude less than 0.7. For each of these intervals, we compute the energy decay rate, ϵ_{vK}, using the generalized version of the von Kármán law (Equation (4)). The cascade rates, ϵ_{PP98}, are then estimated using the Politano–Pouquet law for the inertial range. From the plot of ϵ_{vK} versus ϵ_{PP98} shown in Figure 2, we see that these rates are in close agreement with each other, indicating a near-lossless transfer of energy from the energy-containing range to the inertial range. The agreement between PP98 and von Kármán rates is strong for most of the intermediate range, but appears to asymptote for higher or lower values. This could possibly be due to the loss of cascade through other channels not taken into account in either of these formalisms. As an example, at very strong total cascade rates, the Politano–Pouquet formalism, which assumes incompressible turbulence, might not account for the full transfer rate, if the compressive channels are carrying an increasing fraction of the energy flux. On the other hand, very low cascade rates might be associated with no steady condition or low effective Reynolds numbers, either of which could invalidate the Politano–Pouquet relations. The proximity of these estimates suggests a quasi-steady, scale-invariant energy cascade.

5. MHD-scale Energy Transfer Drives Dissipation

Having established that $\epsilon_{vK} \approx \epsilon_{PP98}$ in a statistical sense, we now address whether all of the energy transferred from large scales (ϵ) is accounted for by the kinetic dissipation, as measured by the pressure–strain rate. Under the assumption of stationarity, the decay rate at large scales is related to the rate of heating as $dZ^2/dt = Q_i + Q_e$. Here, we assume that protons and
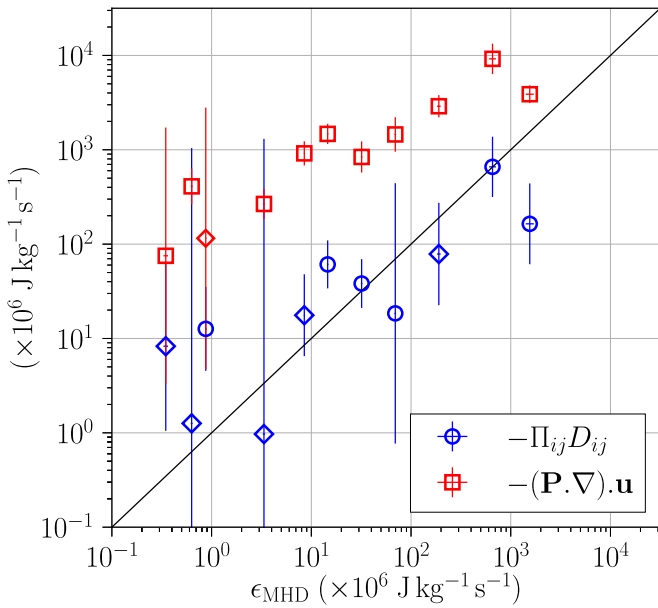
Figure 3. Comparison of average values of $-\Pi_{ij}D_{ij}/\rho$ and $-(\mathbf{P} \cdot \nabla) \cdot \mathbf{u}/\rho$ with the energy decay rates estimated at MHD scales for the collection of MMS intervals. Note that the factors of mass density ρ are used to convert energy per unit volume to energy per unit mass, the latter being the standard units used in incompressible turbulence theory. The computed rates have been accumulated into 11 bins and the average in each bin has been shown; positive values are represented using circles and negative values using diamond markers.

electrons are the only species present, and $Q_i = \partial_t \langle \mathcal{E}_i^{th} \rangle$ and $Q_e = \partial_t \langle \mathcal{E}_e^{th} \rangle$ are their respective heating rates. Simulations have already established this (see Figure 1), but here we study whether the same correspondence is supported in in situ data.

In observation, it is not possible to follow the time evolution of an isolated plasma parcel, so we resort to an indirect method to quantify the relation of MHD-scale transfer and dissipation. We hypothesize that

$$\epsilon \approx Q_i + Q_e = -(\mathbf{P} \cdot \nabla) \cdot \mathbf{u}. \quad (6)$$

The kinetic simulation results shown in Figure 1 support this (also see Pezzi et al. 2019; Bandyopadhyay et al. 2020). Now, we carry out a statistical survey of the MMS magnetosheath samples to compare the MHD-scale energy transfer rates (ϵ) with pressure–strain heating rates ($-(\mathbf{P} \cdot \nabla) \cdot \mathbf{u}$).

Since Figure 2 showed $\epsilon_{vK} \approx \epsilon_{PP98}$, in the following analysis, we define $\epsilon_{MHD} = (\epsilon_{vK} + \epsilon_{PP98})/2$ to be the energy transfer rates at MHD scales. In Figure 3, we employ MMS data to compute the average incompressive heating rates (measured by $-\Pi_{ij}D_{ij}$) and the average total dissipation rates, represented by $-(\mathbf{P} \cdot \nabla) \cdot \mathbf{u}$ in bins of the MHD flux values, ϵ_{MHD}. In Figure 3, we have used 12 bins to divide the data into but the very last bin does not have any data points, which is why only 11 points are shown. Although both $-\Pi_{ij}D_{ij}$ and $-(\mathbf{P} \cdot \nabla) \cdot \mathbf{u}$ increase with ϵ_{MHD}, the incompressive heating rate values, $-\Pi_{ij}D_{ij}$, lie close to the equality line. This is possibly because both the von Kármán law (Equation (4)) and the third-order-based formalism, as written in Equation (5), are based on incompressible MHD theories and therefore do not take into account the compressible effects. We note that, in recent years, several studies have extended the incompressible third-order law to include compressible effects (e.g., Banerjee & Galtier 2013; Hadid et al. 2018; Andrés et al. 2021). However, these

extensions use some form of approximate closure, e.g., adiabatic or isothermal, and we choose not to introduce such additional complications at this time. In the next sections, we study the relative ion and electron heating rates and what controls them.

6. Ion versus Electron Heating

Following Matthaeus et al. (2016), we now investigate how the proton dissipation responds to the strength of the cascade. A number of studies of solar wind turbulence suggest that a stronger cascade coming from larger MHD scales leads to enhanced dissipation near proton scales (Smith et al. 2006; Matthaeus et al. 2008). Based on a Kolmogorov phenomenology, one expects that a larger cascade rate (ϵ) increases the magnitude of the small-scale fluctuations. Specifically, on average the fluctuation amplitude δB_ℓ at length ℓ scales as $\delta B_\ell \sim \epsilon^{1/3} \ell^{-2/3}$. So near the ion scales $\ell = d_i$, the turbulent fluctuations increase as $\epsilon^{1/3}$. A larger amplitude causes a stronger perturbation to proton orbits, which increases proton dissipation, leaving less energy available for heating of electrons. In particular, under favorable circumstances (see Dmitruk et al. 2004a; Dalena et al. 2014; Parashar et al. 2014, and Chandran et al. 2010 for examples) perturbations at the proton scale will produce variations of the perpendicular electric field that cause a net increase in particle energy during each gyroperiod.

We may formulate this zeroth-order expectation as

$$\frac{Q_i}{Q_e} \sim \epsilon^{1/3} \approx (Q_i + Q_e)^{1/3}. \quad (7)$$

Having identified heating rates with the pressure–strain rates, we can test these relations in in situ data. Using the same ensemble of MMS magnetosheath and particle-in-cell (PIC) simulation data, we test this hypothesis. The MMS and simulation results are illustrated in Figure 4. The 2.5D PIC simulations were performed using the P3D (Zeiler et al. 2002) code. Additionally, we use a solar wind data point and a single point from a 3D PIC simulation (Roytershteyn et al. 2015), performed using the VPIC code (Bowers et al. 2008). Details of the specific simulation runs are given in Appendix A. For the solar wind data point, the relative ion–electron heating rate is taken as $Q_i/Q_e = 1.5$ (Cranmer et al. 2009), and the total heating rate as $Q_i + Q_e = 10^4$ W kg^{-1} (Vasquez et al. 2007).

In Figure 4, the data were divided into seven bins but there was no data point in the very last bin, which is why only six points are shown on the plot.

There is a general trend for increased relative heating of protons compared to heating of electrons in runs that have larger total heating. Further, both the simulation and MMS data sets are roughly consistent with the scaling predicted in Equation (7). While the data, especially the simulation points in Figure 4, are not inconsistent with the proposed scaling, the scatter observed in both data groupings motivates examination of the influence of additional parameters.

Note that although some previous simulations showed an increase in the ratio of proton to electron heating rate with the total dissipation rate (Wu et al. 2013; Matthaeus et al. 2016; Hughes et al. 2017), this is the first time the 1/3 slope scaling dependence is demonstrated. Additionally, this is the first study to use in situ data to support this scaling.
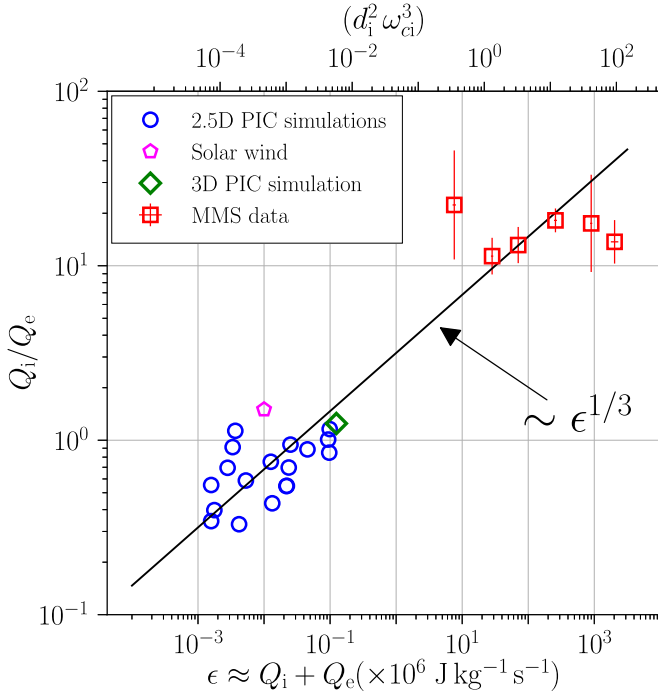
Figure 4. Ratio of proton to electron heating rate vs. total (proton + electron) heating rate. For MMS results, $-\Pi_{ij}D_{ij}$ (averaged over each interval), identified as the heating rate (i.e., $Q_s = -\Pi_{ij}^{(s)}D_{ij}^{(s)}$), is shown by red squares. The total and relative heating rates were accumulated into six bins, and the averages in these bins are shown here. Only intervals with positive ion and electron heating rate were considered. The points indicate that the relative heating of protons increases with the total heating rate (the solid line, with a slope of 1/3, is given for reference). The horizontal axis has been normalized using the typical values for the magnetosheath: $d_i = 10$ km and $\omega_{ci} = 0.6$ Hz.

7. Partitioning of Heating and Timescales

Matthaeus et al. (2016) argued that the ratio of ion to electron heating rate is approximately proportional to the ratio of ion cyclotron time to nonlinear timescale at the ion scale. The theoretical argument was given as follows. It is reasonable to hypothesize that the effective transfer of energy between fluid motion or electromagnetic field and random thermal motions of particles occurs through disruption of perpendicular gyromotion. The effectiveness of this disruption depends on the degree to which the magnetic field at the scale of the particle gyro-orbit changes during a gyroperiod (τ_{ci}). The typical time for the magnetic field fluctuations at scale ℓ to change significantly can be estimated using the nonlinear time $\tau_{nl}(\ell)$ as

$$\tau_{nl}(\ell) = \frac{\ell}{\delta B_\ell}. \quad (8)$$

The simplest choice for proton kinetic scale ℓ is the ion inertial scale d_i, which is typically associated (up to factors of a few) with the spectral break of the turbulent spectrum (Leamon et al. 1998) as well as the typical current sheet thicknesses in turbulent plasmas (Shay et al. 1998; Brown et al. 2006). Consequently, the degree of perturbation during a gyroperiod is related to the quantity $\tau_{ci}/\tau_{nl}(d_i)$. Therefore, we adopt the hypothesis that the heating rate of protons versus that of electrons is sensitive to the ratio of proton cyclotron time to nonlinear timescale at the ion inertial scale, so that

$$\frac{Q_i}{Q_e} \sim \frac{\tau_{ci}}{\tau_{nl}(d_i)}. \quad (9)$$
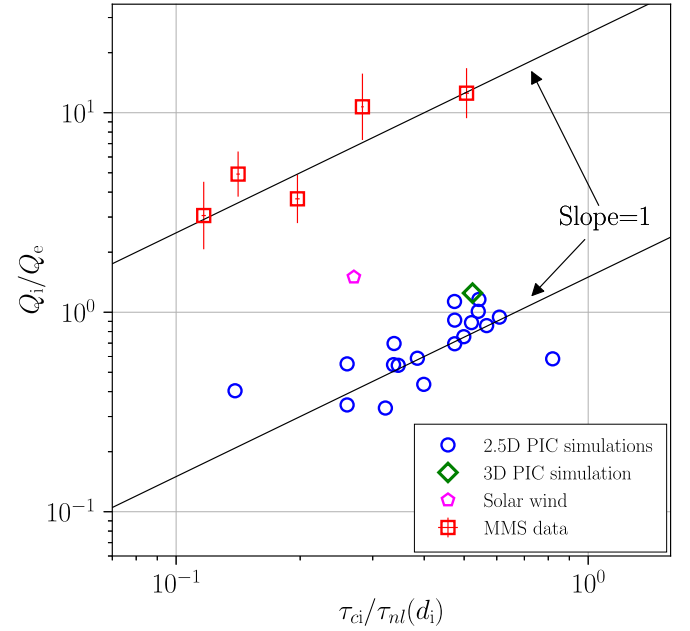
Figure 5. Relative proton–electron heating (Q_i/Q_e) vs. ratio of the ion cyclotron time (τ_{ci}) to the nonlinear time (τ_{nl}) evaluated at d_i. For the MMS data, we identify $-\Pi_{ij}D_{ij}$ as the heating rate, $Q_s = -\Pi_{ij}^s D_{ij}^s$. Only intervals with positive ion and electron heating rates were considered. The two solid lines are parallel and have slopes of unity.

We test this hypothesis using the PIC simulation and MMS database used in the analyses reported above. In Figures 4 and 5, we use intervals where both the ion and electron heating rates are positive. The fraction of intervals where either one of these rates was found to be negative is around 2/3. This leaves us with about 350 intervals. Figure 5 shows that the relative proton–electron heating rate increases with the ratio $\tau_{ci}/\tau_{nl}(d_i)$. This increasing trend with the timescale ratio is supported by both the simulation and MMS data shown. However, the two groups of data values lie on different levels, suggesting a dependence on additional parameters.

8. Variation with Plasma Beta

In the previous section, we ignored the dependence of Q_i/Q_e on β. However, the evidence for this dependence can be seen clearly from Figure 5, where the MMS observations, with $\beta_p \sim 10$, and the simulation data points, with $\beta_p \sim 1$, separate into two distinct populations. A variation with plasma beta was anticipated in Matthaeus et al. (2016). Several hybrid-simulation studies explored this beta variation in both low and high beta regimes (Kawazura et al. 2019; Cerri et al. 2021; Arzamasskiy et al. 2022). Here, we extend to fully kinetic simulations and in situ observations. We proceed by plotting heating ratio from the MMS observations and the 2.5D PIC simulation data as a function of proton beta. The nominal parameters used for computing the relevant quantities in the solar wind are taken as mean magnetic field $B_0 = 3$ nT (Verscharen et al. 2019), turbulence amplitude $\delta B = 22.36$ km s^{-1} (Breech et al. 2008), correlation length $\lambda_c = 10^6$ km, ion inertial length $d_i = 100$ km, and plasma beta $\beta_p = 1.05$ (Wilson et al. 2018). Using these values, we obtain $\tau_{ci}/\tau_{nl}(d_i) = 0.27$.

We can include the beta dependence by writing $Q_i/Q_e = c(\beta)\tau_{ci}/\tau_{nl}(d_i)$, where the explicit functional form of
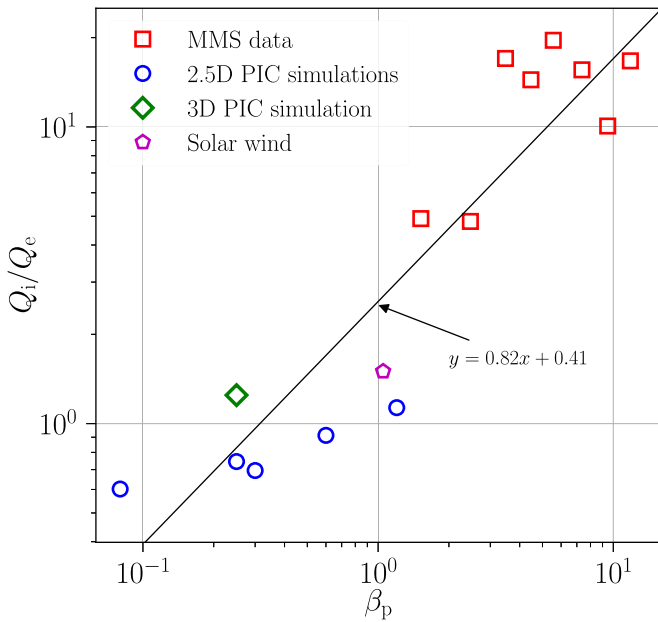
Figure 6. Relative proton–electron heating (Q_i/Q_e) vs. proton plasma beta, β_p. Many data points from the 2.5D PIC simulation have the same β_p, where the average Q_i/Q_e is shown.

Figure 7. Relative proton–electron heating (Q_i/Q_e) vs. $c(\beta)\tau_{ci}/\tau_{nl}(d_i)$.

$c(\beta)$ is not known. Figure 6 plots the heating ratio Q_i/Q_e as a function of proton beta β_p. From the points in the figure, possibly a complicated functional form can be obtained. However, here we assume that τ_{ci}/τ_{nl} is independent of β, and for simplicity, adopt a simple functional form $c(\beta) = A\beta^m$. On performing a fit to all the data points, we obtain $A = 10^{0.41} = 2.57$ and $m = 0.82$. Thus, a simple functional form of $c(\beta)$ is obtained as $c(\beta) = 2.57\beta^{0.82}$, as illustrated in Figure 6.

9. Total Variation

Using the functional form for $c(\beta)$ found in the previous section, we can write

$$\frac{Q_i}{Q_e} = c(\beta)\frac{\tau_{ci}}{\tau_{nl}(d_i)}, \tag{10}$$

$$c(\beta) = 2.57\beta^{0.82}. \tag{11}$$

To test the validity of this result, we plot Q_i/Q_e versus $c(\beta)\tau_{ci}/\tau_{nl}$, with $c(\beta) = 2.57\beta^{0.82}$. As we can see from Figure 7, the MMS data points and the 2.5D simulation data points are in excellent agreement with this result.

10. Discussion

The above results present a scenario connecting plasma heating with energy transfer and cascade at the larger scales. We have not assumed any particular dissipation mechanism. Rather, here we focus on the energetics, and the regionally averaged rate of conversion into internal energy. This general formulation subsumes, in principle, all available mechanisms, except non-Vlasov processes that involve particle correlations, such as collisions.

For a proper perspective, it is important to recognize that there have been a number of previous studies that estimate the partitioning of internal energy according to particle species, and in particular, protons and electrons. An elementary approach to

understanding this differential heating is to examine the condition for cyclotron resonance (mainly of protons) including helicity signatures (Leamon et al. 1998, 2000). In this approach non-cyclotron heating is often assumed to be due to Landau damping (Leamon et al. 1998b, 1999). This reasoning is often supplemented by an assumption that the cascade from large to smaller scales is first damped by protons (Verma et al. 1995), and the remaining cascade damps on electrons and smaller scales (Stawarz et al. 2009). An extensive discussion of the relations of cascade to species-dependent dissipation and heating is given by Vasquez et al. (2007). Several studies have previously explored the dependence of electron heating on other parameters such as turbulence amplitude (Gary et al. 2012), plasma beta (Chang et al. 2013), and ion-to-electron mass ratio (Gary et al. 2016), as well as the variation of the relative ion–electron heating with the temperature ratio of the species (Parashar & Gary 2019). There have also been attempts to provide analytical estimates for Q_i/Q_e from simulations (Quataert 1998; Howes 2010; Kawazura et al. 2019) as functions of the ion-to-electron temperature ratio, T_i/T_e and the ion plasma beta, β_i. We provide a comparison of these models with our results in Appendix B. It is also possible to employ observations over a range of heliocentric distances to infer the branching ratio of proton and electron heating in a semiempirical determination (Cranmer et al. 2009). Moving toward more detailed models, specific models for perpendicular heating of protons (Dmitruk et al. 2004b; Chandran et al. 2010) have received considerable support. Full differential heating models based on phenomenological theories such as critical balance have also been developed (Howes 2010, 2011). In assessing how these various approaches stand in relation to one another, it is important to take into account the sometimes nuanced relationships between cascade, dissipation, temperature, and production of heat (see, e.g., Matthaeus et al. 2020).

Recent related studies of pressure–strain rate in reconnection regions have shown that electron heating is stronger than ion heating for reconnection (Bandyopadhyay et al. 2021; Zhou et al. 2021). However, global dissipation can often be stronger

for ions than electrons, as shown here (Figures 4 and 5). This is particularly true for magnetosheath observations. This behavior indicates that reconnection alone possibly does not control the total dissipation (Hou et al. 2021), and other dissipation processes may also play important roles in dissipating turbulent fluctuations. This is rather surprising, because small-scale reconnection, occurring in thin current sheets, is often considered as a natural component of turbulent cascade (Servidio et al. 2009). But it is evidently not the only relevant component.

There are several features of the present study that require additional comments, and possibly additional study. For example, for the present magnetosheath observations both $-(\boldsymbol{P} \cdot \nabla) \cdot \boldsymbol{u}$ and $-\Pi_{ij} D_{ij}$ exhibit approximately linear proportional scaling with the MHD energy transfer rate, over about three orders of magnitude, as illustrated in Figure 3. However, while the incompressive component $-\Pi_{ij} D_{ij}$ maintains an approximate equality with ϵ_{MHD}, the total pressure–strain interaction $-(\boldsymbol{P} \cdot \nabla) \cdot \boldsymbol{u}$ does not; rather it resides roughly at an order of magnitude higher. This relationship may be anticipated to some degree, as mentioned in Section 5, when one recalls that the horizontal axis—the average of transfer rates under the third-order law and von Kármán decay rates—is principally an incompressive rate, while the $-(\boldsymbol{P} \cdot \nabla) \cdot \boldsymbol{u}$ term measures total conversion of energy from both compressive and incompressive channels. However, there are additional possible contributions to $-(\boldsymbol{P} \cdot \nabla) \cdot \boldsymbol{u}$ that might not be represented in corresponding contributions to the MHD transfer rate measured at larger scales. In particular, by analysis of the scale-dependent von Kármán–Howarth equations (Antonia & Burattini 2006; Hellinger et al. 2018) one understands that such deviations from equality of dissipative and MHD transfer rates can arise due to incomplete separation of scales. In particular, if the scale-resolved dissipation is not confined to lengths much smaller than the scales at which the third-order law is evaluated, then the nonlinear transfer rate will not correspond to the total dissipation rate (Yang et al. 2022). Time dependence at the intermediate scales can also contribute to this deficit. These caveats are equivalent to the statement that a pristine inertial range requires full separation of scales as well as time independence of the scales at which the transfer is measured, i.e., the assumption of time-stationarity. Perhaps, too often these requirements (already explicit in Kolmogorov's reasoning) are not subject to adequate scrutiny once the weaker requirement of a well defined power-law energy spectrum is observed. In the present case the significant inequality between $-(\boldsymbol{P} \cdot \nabla) \cdot \boldsymbol{u}$ and $-\Pi_{ij} D_{ij}$, while $-\Pi_{ij} D_{ij}$ corresponds well to MHD "inertial range" transfer, hints at the possibility that the magnetosheath intervals we are examining do not attain true inertial range conditions at the scales of our analysis. This possibility, and the associated hypothesis that compressive heating is indeed occurring at intermediate scales, will be further studied in subsequent research.

Keeping in mind the above several reasons for potential departures from pristine cascade conditions, we have also developed here some specific results regarding partitioning of increases in internal energy (heating) between protons and electrons. This issue has remained a central question in heliospheric physics and astrophysics due to the impact of this branching ratio on phenomena such as acceleration of solar and stellar winds (Hundhausen 1972; Cranmer et al. 2009). Here we used our collection of kinetic simulations and an ensemble of MMS magnetosheath observations to develop an empirical scaling based on the analytical model presented by Matthaeus et al. (2016). In particular we demonstrated the dependence of the proton–electron heating ratio on the ratio of cyclotron time to nonlinear timescale, and further determined empirically the additional dependence on plasma beta. The main result, embodied in Equation (10), amounts to a specific realization of the functional form for the proton–electron heating ratio (Matthaeus et al. 2016). It remains to be seen if there are additional parametric variations of this result that were not explored using the available simulation and spacecraft data sets. For example, it is possible that the heating ratio might also vary with effective Reynolds number or, equivalently, system size (Parashar et al. 2015).

Appendix A
PIC Simulation Details

Our analysis employs results from multiple 2.5D PIC simulations and results from one 3D PIC simulation. The 2.5D simulations were performed using the fully electromagnetic PIC code P3D (Zeiler et al. 2002) in periodic 2.5D geometry (three component vectors on a 2D spatial grid). The simulations solve the Vlasov–Maxwell equations with no external driving in a periodic box.

The 2.5D simulation of Figure 1 was performed in a domain with dimension of $L = 149.6 \, d_{\mathrm{i}}$, where d_{i} is the ion inertial length, and 4096^2 grid points and 3200 particles per cell ($\sim 10^{11}$ total particles). The ion-to-electron mass ratio is $m_{\mathrm{i}}/m_{\mathrm{e}} = 25$, and the ratio of electron plasma frequency to the electron cyclotron frequency is $\omega_{\mathrm{pe}}/\omega_{\mathrm{ce}} = 3$. The run was started with uniform number density $n_0 = 1.0$ and Maxwellian-distributed ions and electrons with temperature $T_0 = 0.3$. A uniform magnetic field $B_0 = 1.0$ is directed out of the plane, and the proton beta value is $\beta_{\mathrm{p}} = 0.6$. This simulation was also used in Parashar et al. (2018) and for a von Kármán analysis of this simulation across different scales; see Adhikari et al. (2021).

To carry out the 3D PIC simulation, the general-purpose plasma simulation code VPIC (Bowers et al. 2008) was used, which solves the relativistic Vlasov–Maxwell equations using a PIC algorithm. The simulation was conducted in a fully periodic three-dimensional domain of size $L = 42 d_{\mathrm{i}}$, with 2048^3 cells. The average number of particles per cell per species was 150, corresponding to approximately 2.6×10^{12} simulation particles. The ion-to-electron mass ratio is $m_{\mathrm{i}}/m_{\mathrm{e}} = 50$, and $\omega_{\mathrm{pe}}/\omega_{\mathrm{ce}} = 2$. The total plasma beta is $\beta_0 = 0.5$.

The parameters of the rest of the simulations, shown in Figures 4 and 5, are given in Table 1. All the runs except the ones with box length of $149.6 \, d_i$ were used in Matthaeus et al. (2016). The 3D PIC run was used in Roytershteyn et al. (2015) and Yang et al. (2022).

Table 1
Parameters of PIC Simulation Runs

Dimension	β_i	β_e	Z_0	B_0	L	$N_x = N_y$	Q_i/Q_e	$Q_i + Q_e$	τ_{ci}/τ_{nl}	ppc
2.5D	0.08	0.08	3.131	5	1.28	64	0.584	⋯	0.82	200
2.5D	0.08	0.08	2.334	5	2.56	128	0.887	2.00E-03	0.521	200
2.5D	0.08	0.08	2.085	5	5.12	256	0.435	6.16E-04	0.399	200
2.5D	0.08	0.08	2.017	5	10.28	512	0.331	1.94E-04	0.322	200
2.5D	0.08	0.08	2	5	20.48	1024	0.343	7.33E-05	0.26	200
2.5D	0.08	0.08	2.031	5	20.48	1024	0.551	7.33E-05	0.26	200
2.5D	0.08	0.08	3.041	5	20.48	1024	0.588	2.46E-04	0.385	200
2.5D	0.08	0.08	4.052	5	20.48	1024	0.754	5.86E-04	0.499	200
2.5D	0.08	0.08	5.064	5	20.48	1024	0.945	1.16E-03	0.609	200
2.5D	0.25	0.25	0.986	5	25.6	2048	0.404	8.19E-05	0.139	400
2.5D	0.25	0.25	2.464	5	25.6	2048	0.542	1.00E-03	0.346	400
2.5D	0.25	0.25	3.942	5	25.6	2048	0.857	4.50E-03	0.567	400
2.5D	0.25	0.25	2.456	5	25.6	2048	0.697	1.10E-03	0.338	400
2.5D	0.25	0.25	3.93	5	25.6	2048	1.159	4.57E-03	0.543	400
2.5D	0.25	0.25	2.456	5	25.6	2048	0.546	1.02E-03	0.337	400
2.5D	0.25	0.25	3.93	5	25.6	2048	1.01	4.33E-03	0.541	400
2.5D	0.3	0.3	0.135	1	149.6	4096	0.695	1.30E-04	0.4742	3200
2.5D	0.6	0.6	0.135	1	149.6	4096	0.913	1.55E-04	0.4743	3200
2.5D	1.2	1.2	0.135	1	149.6	4096	1.132	1.70E-04	0.4738	3200
3D	0.25	0.25	0.707	0.5	42	2048	1.2474	1.44E-05	0.524	150

Note. The box lengths are described in the L column and the grid described in the $N_x = N_y$ column. Listed are proton beta β_i, electron beta β_e, turbulence amplitude Z_0, out-of-plane uniform magnetic field B_0, box size L, grid points in the plane $N_x = N_y = N_z$ (for 3D), the ratio of average ion to electron heating rates Q_i/Q_e, the sum of ion and electron heating rates $Q_i + Q_e$, the ratio of proton cyclotron time to nonlinear time at ion inertial scale (d_i) τ_{ci}/τ_{nl}, the number of particles per cell ppc. All lengths are normalized to d_i. The total heating rate, $Q_i + Q_e$, is in units of $d_i^2 \omega_{ci}^3$ for the 2.5D simulations, and in units of $d_e^2 \omega_{pe}^3$ for the 3D simulation.

Appendix B
Comparison with Other Models

We compare our results in Figure 6 with models that predict Q_i/Q_e as proposed by Quataert (1998), Howes (2010), and Kawazura et al. (2019). Quataert (1998) considers the dissipation of Alfvénic turbulence in hot astrophysical plasmas (such as accretion flows) occurring through transit-time damping. The proposed model is given by

$$\frac{Q_i}{Q_e} = \sqrt{\frac{m_i T_i}{m_e T_e}} \exp\left[-\left(1 + \frac{T_e}{T_i}\right)\beta^{-1}\right]. \quad (B1)$$

Howes (2010), on the other hand, calculates the dissipation based on a cascade model of Alfvénic turbulence. This model agrees with the Quataert (1998) model for low values of β_i, but starts deviating significantly for $\beta_i \gtrsim 1$:

$$\frac{Q_i}{Q_e} = c_1 \frac{c_2^2 + \beta_i^p}{c_3^2 + \beta_i^p} \sqrt{\frac{m_i T_i}{m_e T_e}} e^{-1/\beta_i}, \quad (B2)$$

where $c_1 = 0.92$, $c_2 = 1.6/(T_i/T_e)$, $c_3 = 18 + 5\log(T_i/T_e)$, and $p = 2 - 0.2\log(T_i/T_e)$. The third model we looked at was due to Kawazura et al. (2019). In this case, they used a hybrid gyrokinetic code to simulate the turbulent heating in a proton–electron plasma over a broad range of β_i and T_i/T_e values. From these simulations, they found a fitting formula for the ion-to-electron heating ratio, which is given below. They note that this relation is approximately insensitive to the ion-to-
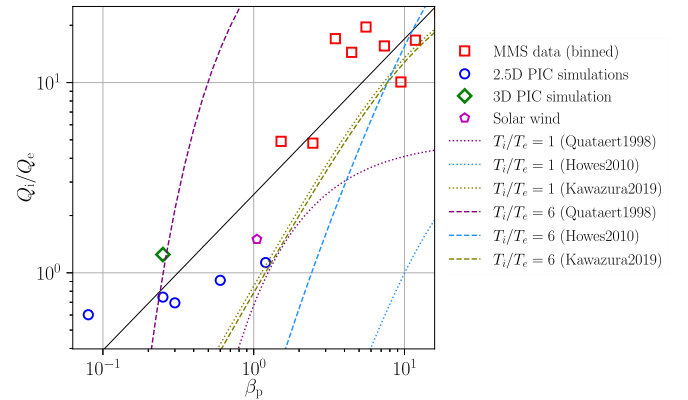
Figure 8. Relative proton–electron heating (Q_i/Q_e) vs. the proton plasma beta (β_p). The data points from various sources are compared with heating models proposed by Quataert (1998), Howes (2010), and Kawazura et al. (2019) for $T_i/T_e = 1$ and 6.

electron temperature ratio T_i/T_e.

$$\frac{Q_i}{Q_e} = \frac{35}{1 + (\beta_i/15)^{-1.4} e^{-0.1 T_e/T_i}} \quad (B3)$$

We find that out of these three models, the one proposed by Kawazura et al. (2019) agrees the best with our results as shown in Figure 8.

ORCID iDs

S. Roy ⓘ https://orcid.org/0000-0003-3891-5495
R. Bandyopadhyay ⓘ https://orcid.org/0000-0002-6962-0959
Y. Yang ⓘ https://orcid.org/0000-0003-2965-7906

T. N. Parashar (ORCID) https://orcid.org/0000-0003-0602-8381
W. H. Matthaeus (ORCID) https://orcid.org/0000-0001-7224-6024
S. Adhikari (ORCID) https://orcid.org/0000-0003-2160-7066
V. Roytershteyn (ORCID) https://orcid.org/0000-0003-1745-7587
A. Chasapis (ORCID) https://orcid.org/0000-0001-8478-5797
Hui Li (ORCID) https://orcid.org/0000-0002-4839-4614
D. J. Gershman (ORCID) https://orcid.org/0000-0003-1304-4769
J. L. Burch (ORCID) https://orcid.org/0000-0003-0452-8403

References

Adhikari, S., Parashar, T. N., Shay, M. A., et al. 2021, PhRvE, 104, 065206
Afshari, A. S., Howes, G. G., Kletzing, C. A., Hartley, D. P., & Boardsen, S. A. 2021, JGRA, 126, e2021JA029578
Andrés, N., Sahraoui, F., Hadid, L. Z., et al. 2021, ApJ, 919, 19
Antonia, R. A., & Burattini, P. 2006, JFM, 550, 175
Arzamasskiy, L., Kunz, M. W., Squire, J., Quataert, E., & Schekochihin, A. A. 2022, arXiv:2207.05189
Bandyopadhyay, R., Chasapis, A., Matthaeus, W. H., et al. 2021, PhPl, 28, 112305
Bandyopadhyay, R., Matthaeus, W. H., Oughton, S., & Wan, M. 2019, JFM, 876, 5
Bandyopadhyay, R., Matthaeus, W. H., Parashar, T. N., et al. 2020, PhRvL, 124, 255101
Bandyopadhyay, R., Oughton, S., Wan, M., et al. 2018, PhRvX, 8, 041052
Banerjee, S., & Galtier, S. 2013, PhRvE, 87, 013019
Barnes, A. 1979, in Solar System Plasma Physics, vol. I ed. E. N. Parker, C. F. Kennel, & L. J. Lanzerotti (Amsterdam: North-Holland), 251
Batchelor, G. K. 1953, The Theory of Homogeneous Turbulence (Cambridge: Cambridge Univ. Press)
Bowers, K. J., Albright, B. J., Yin, L., Bergen, B., & Kwan, T. J. T. 2008, PhPl, 15, 055703
Braginskii, S. I. 1965, RvPP, 1, 205
Breech, B., Matthaeus, W. H., Minnie, J., et al. 2008, JGRA, 113, A08105
Brown, M. R., Cothran, C. D., & Fung, J. 2006, PhPl, 13, 056503
Bruno, R., & Carbone, V. 2005, LRSP, 2, 4
Burch, J. L., Moore, T. E., Torbert, R. B., & Giles, B. L. 2016, SSRv, 199, 5
Cerri, S. S. 2016, PhD thesis, Universität Ulm
Cerri, S. S., Arzamasskiy, L., & Kunz, M. W. 2021, ApJ, 916, 120
Chandran, B. D. G., Li, B., Rogers, B. N., Quataert, E., & Germaschewski, K. 2010, ApJ, 720, 503
Chang, O., Gary, S. P., & Wang, J. 2013, JGRA, 118, 2824
Chasapis, A., Yang, Y., Matthaeus, W. H., et al. 2018, ApJ, 862, 32
Chen, C. H. K., Klein, K. G., & Howes, G. G. 2019, NatCo, 10, 740
Cranmer, S. R., Matthaeus, W. H., Breech, B. A., & Kasper, J. C. 2009, ApJ, 702, 1604
Dalena, S., Rappazzo, A. F., Dmitruk, P., Greco, A., & Matthaeus, W. H. 2014, ApJ, 783, 143
de Kármán, T., & Howarth, L. 1938, RSPSA, 164, 192
Del Sarto, D., & Pegoraro, F. 2017, MNRAS, 475, 181
Del Sarto, D., Pegoraro, F., & Califano, F. 2016, PhRvE, 93, 053203
Dmitruk, P., Matthaeus, W. H., & Lanzerotti, L. J. 2004a, GeoRL, 31, 21805
Dmitruk, P., Matthaeus, W. H., & Seenu, N. 2004b, ApJ, 617, 667
Dunlop, M. W., Southwood, D. J., Glassmeier, K.-H., & Neubauer, F. M. 1988, AdSpR, 8, 273
Freidberg, J. P. 1982, RvMP, 54, 801
Gary, S. P., Chang, O., & Wang, J. 2012, ApJ, 755, 142
Gary, S. P., Hughes, R. S., & Wang, J. 2016, ApJ, 816, 102
Gary, S. P., Thomsen, M. F., Yin, L., & Winske, D. 1995, JGRA, 100, 21961
Goldstein, M. L., Roberts, D. A., & Matthaeus, W. H. 1995, ARA&A, 33, 283
Hadid, L. Z., Sahraoui, F., Galtier, S., & Huang, S. Y. 2018, PhRvL, 120, 055102
Hellinger, P., Verdini, A., Landi, S., Franci, L., & Matteini, L. 2018, ApJL, 857, L19
Hoppock, I. W., Chandran, B. D. G., Klein, K. G., Mallet, A., & Verscharen, D. 2018, JPlPh, 84, 905840615
Hossain, M., Gray, P. C., Pontius, D. H., Matthaeus, W. H., & Oughton, S. 1995, PhFl, 7, 2886
Hou, C., He, J., Zhu, X., & Wang, Y. 2021, ApJ, 908, 237
Howes, G. G. 2010, MNRAS, 409, L104
Howes, G. G. 2011, ApJ, 738, 40
Hughes, R. S., Gary, S. P., Wang, J., & Parashar, T. N. 2017, ApJL, 847, L14
Hundhausen, A. J. 1972, Coronal Expansion and Solar Wind (New York: Springer)

Isenberg, P. A., Lee, M. A., & Hollweg, J. V. 2001, JGR, 106, 5649
Kawazura, Y., Barnes, M., & Schekochihin, A. A. 2019, PNAS, 116, 771
Kolmogorov, A. N. 1941, DoSSR, 32, 16
Leamon, R. J., Matthaeus, W. H., Smith, C. W., et al. 2000, ApJ, 537, 1054
Leamon, R. J., Matthaeus, W. H., Smith, C. W., & Wong, H. K. 1998b, ApJL, 507, L181
Leamon, R. J., Smith, C. W., Ness, N. F., Matthaeus, W. H., & Wong, H. K. 1998, JGR, 103, 4775
Leamon, R. J., Smith, C. W., Ness, N. F., & Wong, H. K. 1999, JGR, 104, 22331
Li, H., Jiang, W., Wang, C., et al. 2020, ApJL, 898, L43
Lichko, E., Egedal, J., Daughton, W., & Kasper, J. 2017, ApJL, 850, L28
Linkmann, M. F., Berera, A., McComb, W. D., & McKay, M. E. 2015, PhRvL, 114, 235001
MacBride, B. T., Forman, M. A., & Smith, C. W. 2005, in ESA Special Pub. 592, Solar Wind 11/SOHO 16, Connecting Sun and Heliosphere, ed. B. Fleck, T. H. Zurbuchen, & H. Lacoste (Paris: ESA), 613
MacBride, B. T., Smith, C. W., & Forman, M. A. 2008, ApJ, 679, 1644
Marsch, E. 1991, in Physics of the Inner Heliosphere II. Particles, Waves and Turbulence, ed. R. Schwenn & E. Marsch (Berlin: Springer), 45
Marsch, E. 2006, LRSP, 3, 1
Matthaeus, W. H., Parashar, T. N., Wan, M., & Wu, P. 2016, ApJL, 827, L7
Matthaeus, W. H., & Velli, M. 2011, SSRv, 160, 145
Matthaeus, W. H., Weygand, J. M., Chuychai, P., et al. 2008, ApJL, 678, L141
Matthaeus, W. H., Yang, Y., Wan, M., et al. 2020, ApJ, 891, 101
Monin, A. S., & Yaglom, A. M. 1971, Statistical Fluid Mechanics, Vol. 1 (Cambridge, MA: MIT Press)
Montgomery, D. 1983, JPL Solar Wind Five, Vol. 228 (NASA Conf. Publication) 0.107
Montgomery, D., Armstrong, J. W., Kintner, P., et al. 1980, Report of the NASA Plasma Turbulence Explorer Study Group, Vol. 715-78 (Pasadena, CA: NASA JPL)
Parashar, T. N., & Gary, S. P. 2019, ApJ, 882, 29
Parashar, T. N., Matthaeus, W. H., & Shay, M. A. 2018, ApJL, 864, L21
Parashar, T. N., Matthaeus, W. H., Shay, M. A., & Wan, M. 2015, ApJ, 811, 112
Parashar, T. N., Vasquez, B. J., & Markovskii, S. A. 2014, PhPl, 21, 022301
Paschmann, G., & Daly, P. W. 1998, ISSIR, 1 https://hdl.handle.net/11858/00-001M-0000-0014-D93A-D
Pezzi, O., Liang, H., Juno, J. L., et al. 2021, MNRAS, 505, 4857
Pezzi, O., Yang, Y., Valentini, F., et al. 2019, PhPl, 26, 072301
Politano, H., & Pouquet, A. 1998a, GeoRL, 25, 273
Politano, H., & Pouquet, A. 1998b, PhRvE, 57, R21
Quataert, E. 1998, ApJ, 500, 978
Retinò, A., Sundkvist, D., Vaivads, A., et al. 2007, NatPh, 3, 236
Roytershteyn, V., Karimabadi, H., & Roberts, A. 2015, RSPTA, 373, 20140151
Servidio, S., Matthaeus, W. H., Shay, M. A., Cassak, P. A., & Dmitruk, P. 2009, PhRvL, 102, 115003
Shay, M. A., Drake, J. F., Denton, R. E., & Biskamp, D. 1998, JGR, 103, 9165
Sitnov, M. I., Merkin, V. G., Roytershteyn, V., & Swisdak, M. 2018, GeoRL, 45, 4639
Smith, C. W., Hamilton, K., Vasquez, B. J., & Leamon, R. J. 2006, ApJL, 645, L85
Smith, C. W., Stawarz, J. E., Vasquez, B. J., Forman, M. A., & MacBride, B. T. 2009, PhRvL, 103, 201101
Squire, J., Meyrand, R., Kunz, M. W., et al. 2022, NatAs, 6, 715
Stawarz, J. E., Eastwood, J. P., Phan, T. D., et al. 2022, PhPl, 29, 012302
Stawarz, J. E., Smith, C. W., Vasquez, B. J., Forman, M. A., & MacBride, B. T. 2009, ApJ, 697, 1119
Usmanov, A. V., Goldstein, M. L., & Matthaeus, W. H. 2014, ApJ, 788, 43
Vasquez, B. J., Smith, C. W., Hamilton, K., MacBride, B. T., & Leamon, R. J. 2007, JGRA, 112, A07101
Verma, M. K. 2004, PhR, 401, 229
Verma, M. K., Roberts, D. A., & Goldstein, M. L. 1995, JGRA, 100, 19839
Verscharen, D., Klein, K. G., & Maruca, B. A. 2019, LRSP, 16, 5
Wan, M., Matthaeus, W. H., Roytershteyn, V., et al. 2016, PhPl, 23, 042307
Wan, M., Oughton, S., Servidio, S., & Matthaeus, W. H. 2012, JFM, 697, 296
Wang, Y., Bandyopadhyay, R., Chhiber, R., et al. 2021, JGRA, 126, e29000
Wilson, L. B., III, Stevens, M. L., Kasper, J. C., et al. 2018, ApJS, 236, 41
Wu, P., Wan, M., Matthaeus, W. H., Shay, M. A., & Swisdak, M. 2013, PhRvL, 111, 121105
Yang, Y., Matthaeus, W. H., Parashar, T. N., et al. 2017a, PhRvE, 95, 061201
Yang, Y., Matthaeus, W. H., Parashar, T. N., et al. 2017b, PhPl, 24, 072306
Yang, Y., Matthaeus, W. H., Roy, S., et al. 2022, ApJ, 929, 142
Yang, Y., Wan, M., Matthaeus, W. H., et al. 2018, MNRAS, 482, 4933

Zeiler, A., Biskamp, D., Drake, J. F., et al. 2002, JGRA, 107, 1230

Zenitani, S., Hesse, M., Klimas, A., & Kuznetsova, M. 2011, PhRvL, 106, 195003

Zhou, M., Man, H., Yang, Y., Zhong, Z., & Deng, X. 2021, GeoRL, 48, e96372